Autonomous multi-species environmental gas sensing using drone-based Fourier-transform infrared spectroscopy

Marius Rutkauskas,[1] Martin Asenov,[2] Subramanian Ramamoorthy[2] and Derryck T. Reid[1]*

[1]*Scottish Universities Physics Alliance (SUPA), Institute of Photonics and Quantum Sciences, School of Engineering and Physical Sciences, Heriot–Watt University, Edinburgh EH14 4AS, UK*
[2]*Informatics Forum, University of Edinburgh, Edinburgh, EH8 9AB, UK*
*D.T.Reid@hw.ac.uk

Abstract: Unmanned aerial vehicles (UAVs) – or drones – present compelling new opportunities for airborne gas sensing, in applications such as environmental monitoring, hazardous scene assessment and facilities' inspection. Instrumenting a UAV for this purpose encounters trade-offs between sensor size, weight, power and performance, driving the adoption of lightweight electrochemical and photo-ionisation detectors, but at the expense of speed, selectivity, sensitivity, accuracy, resolution and traceability. Here, we report the design and integration of a broadband Fourier-transform infrared spectrometer with an autonomous UAV, providing ro-vibrational spectroscopy throughout the molecular fingerprint region from $3 - 11$ µm ($3333 - 909$ cm^{-1}) and enabling rapid, quantitative aerial surveys of multiple species simultaneously with an estimated noise-limited performance of 18 ppm (propane). Bayesian interpolation of the acquired gas concentrations is shown to provide both localization of a point source with approximately one metre accuracy, and distribution mapping of a gas cloud, with accompanying uncertainty quantification.

1. Introduction

Atmospheric gas sensing using UAVs is growing in importance because of the wide range of applications this technology can flexibly address, such as climate monitoring [1], pollution detection [2], volcanology [3], industrial site monitoring [4], and hazardous scene assessment such as monitoring wild fires [5]. UAV gas sensing has been used to provide ground-truth validation for Earth-observation satellites [6], to sample humidity at sea-level [7] and to provide horizontal and vertical particulate concentration profiles [8,9]. The benefits over conventional approaches are striking: drones – particularly rotary-wing UAVs – can be deployed quickly at low cost and without the need for dedicated runways, can operate in contaminated or hazardous environments, and can perform systematic high-resolution surveys in three-dimensional space with a repeatability which is impossible for humans.

Despite this potential, practical considerations – typically associated with size, weight and power constraints, but also in some circumstances regulatory compliance – limit the gas sensing capabilities of autonomous UAVs in a number of specific ways. A recent survey of onboard sensing technologies [10] reveals the predominant use of electrochemical [11] / metal-oxide sensors, with a smaller number of laser-line infrared sensors [12]. None of these technologies is broadband and chemically agnostic: the electrolytes used in electrochemical sensors are optimized for certain gases, while laser-line sensors monitor infrared absorption features unique to particular molecules. Although electrochemical sensors are lightweight, they can lack chemical selectivity, with some showing cross-sensitivity to different molecules [13], and their response time is slow (~20 seconds) [14], meaning that their ability to detect a localized gas source during a rapid survey flight is limited. In contrast, Fourier-transform

infrared spectroscopy (FTIR) provides a fast and inherently multi-analyte detection capability, but this advantage has not previously been exploited on UAVs due to the complexity of integrating an interferometric system with sufficiently low payload and power demands, yet possessing a high degree of resilience to vibration and acceleration. Gas absorption spectroscopy of light molecules relies on an FTIR spectrometer with sufficient resolution to resolve individual gas lines – typically a few cm^{-1} or less – and spectral coverage that includes the molecular fingerprint region that falls within the atmospheric transmission window from 8 – 12 µm. While one micro-opto-electro-mechanical systems (MOEMS) Fourier-transform spectrometer was deployed on a fixed-wing UAV [15], there are no reports in the literature of any system offering the required performance. Aside from payload and power considerations, the positioning of an open-path interferometer is made challenging on a UAV, either because of the constraints of the airframe geometry in a fixed-wing aircraft or the turbulence / screening effects associated with the complex air flow around a rotary-wing UAV [16].

In this article we introduce the first intrinsically multi-species gas sensing using a UAV-integrated Fourier-transform spectrometer with long-wavelength infrared spectral coverage extending deep into the molecular fingerprint region. A multi-parameter fit of the in-flight absorption spectra provides GPS-referenced concentration data for carbon dioxide, propane and water (humidity) from which we separately show the localization of point sources of gas and the mapping of a gas distribution. The system performance is characterized under real-world flight conditions.

2. Fourier-transform spectrometer architecture and system integration

Illustrated in Fig. 1, the Fourier-transform spectrometer (FTS) consisted of a Michelson interferometer comprising a CaF$_2$ beamsplitter and two scanning aluminium retroreflectors, each mounted on a separate voice-coil actuator and driven in antiphase by a 3-Hz sinusoidal signal. Black-body radiation from a Kanthal infrared emitter (Helioworks EK3430) was collimated using a parabolic reflector and a ZnSe lens and steered into the interferometer after being combined on a Ge window with a 1550-nm beam from a single-frequency distributed feedback (DFB) laser. This 1550-nm light provided a means of calibrating the optical path difference in the interferometer and was detected after the interferometer by an InGaAs photodiode located behind a second Ge window, leaving the black-body radiation to travel along the sensing path, finally being focused onto a mercury cadmium telluride (MCT) detector (Vigo System PVI-4TE-10.6) by a ZnSe lens. A 250-MHz USB oscilloscope with an onboard waveform generator provided synchronous scanning and 2 MS/s, 14-bit data acquisition under the control of an onboard Nvidia Jetson TX2 computer. The shape of the recorded spectrum (for example, see Fig. 1(e)) was essentially a classical black-body spectrum modulated by the transmission and reflection functions of the component optics and the spectral response curve of the MCT detector.

The FTS was constructed with a view to achieving robust performance while minimising its weight and power consumption and using off-the-shelf components. The optics were mounted in an optical cage system in which carbon fibre tubes were substituted for the standard steel rods, providing comparable stiffness with a considerable weight reduction. The FTS and all of its associated hardware were powered from a 4S (14.8-volt) 4000 mAh (59.2 Wh) LiPo battery pack, the output of which was conditioned using DC-DC converters to meet the different voltage requirements of the thermal emitter, scan-mirror amplifier, oscilloscope, DFB laser diode, MCT detector and spectrometer computer. The total maximum power consumption was 60 W, distributed between the oscilloscope (10 W), voice-coil amplifier (10 W), thermal source (12 W), DFB laser (0.24 W), MCT detector (2.8 W), InGaAs detector (0.03 W), cooling fans (4.8 W) and computer (20 W) allowing the FTS to run for 1 hour with the selected LiPo battery pack.
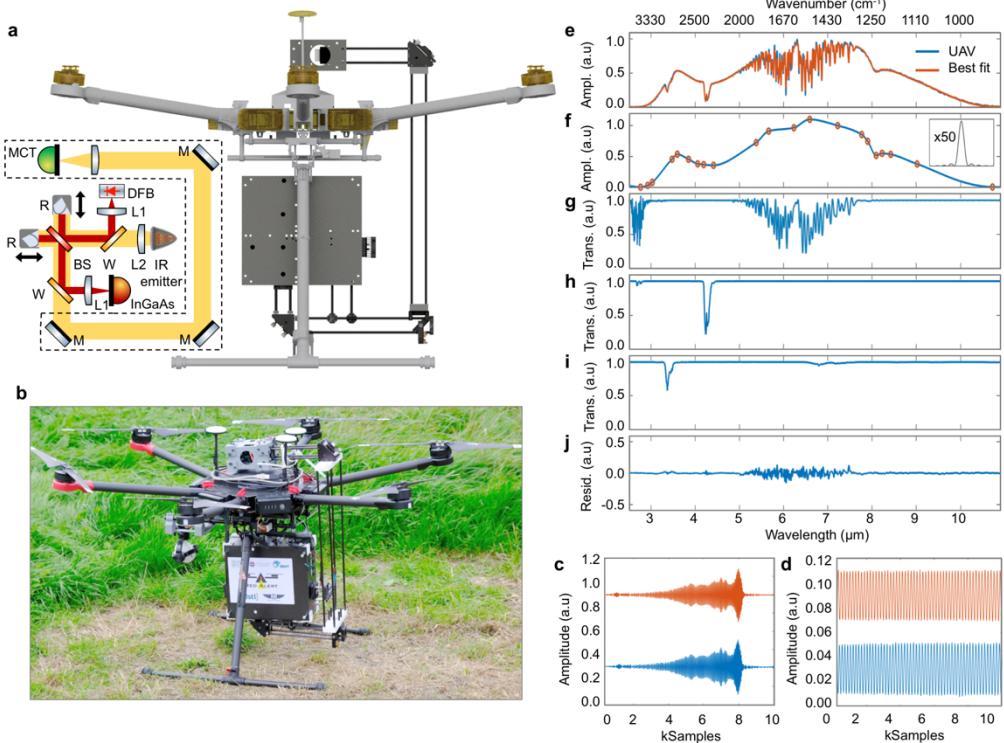
Fig. 1. Optical configuration and in-flight performance data for the UAV-mounted Fourier-transform spectrometer. (a) UAV schematic showing spectrometer suspended underneath, and the C-shaped sensing path (dashed line) of 1 m length. DFB,1550-nm single-frequency laser diode; L1, aspheric lenses (coated for 1.5 µm), L2, ZnSe lenses; BS, CaF$_2$ beamsplitter; W, Ge windows; R, retroreflectors; M, silver mirrors; InGaAs, InGaAs photodiode; MCT, MCT detector. (b) The assembled system in field trials. (c) Representative mid-infrared and (d) reference laser interference fringes obtained from the UAV before take-off (red), and in-flight (blue). (e) Infrared absorption spectrum obtained in flight (blue) and least squares fit (red). (f) Fitted envelope, which is modelled as a spline curve with the positions of the anchor points (symbols) being unconstrained fitting parameters; inset: fitted sinc^2(ν) instrument function, corresponding to the triangular apodization used. (g–i) Fitted transmittance spectra for water, carbon dioxide and propane. These spectra, obtained during a propane sensing flight, show a background CO$_2$ level of 400 ppm and concentrations for water of 1.16% and for propane of 362 ppm. (j) The fitting residual between the two spectra in e, presented on the same scale. Insufficient instrument resolution to resolve the dense and saturated line structure of water in the 5 – 7-µm region leads to the remaining fitting uncertainty here.

The FTS was suspended by springs beneath the DJI M600 drone using carbon-fibre plate and extension springs (Fig. 1(a)), decoupling the vibrations from the hexacopter motors and giving a ground clearance of around 10 cm before take-off. The effectiveness of the vibration isolation is illustrated in Figs. 1(c) and 1(d), which show that the quality of the interference fringes recorded during flight is as high as that before take-off. The weight of whole system was 14.8 kg, which is under the specified maximum lifting weight of the M600 platform (15.2 kg) and allowed an endurance of around 15 minutes. To provide sufficient sensitivity, the optical sensing path was folded in a vertical C shape around the UAV, terminating above the UAV with the MCT detector. This geometry was chosen to permit sensing in the less turbulent region of air above the UAV and avoid the screening effect experienced by a sensor that is entirely underneath the drone [16]. The effective external path length was 1 m.

We implemented a communication pipeline in which data from the spectrometer computer was sent across a UART connection to the UAV flight computer, and then transferred across

a high bandwidth wireless link to an application running on an Android mobile phone connected to the remote controller. The communication pipeline was built using the middleware, ROS (Robot Operating System), a *de facto* standard for developing robotics frameworks. Under the design of the ROS middleware, different nodes (programs) operate by sharing a common communication protocol. Using this paradigm, we implemented modular software components, wherein each separate module was logically independent of the other. This mitigated a wide range of potential problems within the system, such that even if individual modules failed owing to software/hardware issues the rest of the system could continue to operate.

3. Sensor performance characterisations

The instrument function of the spectrometer, shown in Fig. 1(f) and inferred from the spectral fitting procedure (see Section 4.3), indicated a spectral resolution of 5.2 cm^{-1}, sufficient to allow successful multi-species fitting of a complex spectrum. This resolution could be improved by using an actuator with a longer scanning range, at the expense of a longer spectrometer response time. Spectra obtained from the UAV in-flight (e.g. Fig. 1(e)) were used to assess the spectral noise and the repeatability of the gas concentration fitting. The signal:noise ratio, defined as the inverse of the standard deviation of the spectral noise in a region without molecular absorption, was inferred from the residuals of the fitted spectrum (see Section 4.3). For a single spectrum, the residuals of the normalised spectrum in the 3 – 5-µm region showed a standard deviation of 0.94%, corresponding to a peak signal:noise ratio of 20.3 dB. Averaging 700 spectra acquired consecutively under constant conditions reduced the visible noise slightly, lowering the residual standard deviation to 0.8%, a factor of 1.2 improvement in the signal:noise. Relative to ambient levels, concentration changes of 31 ppm (CO_2) and 18 ppm (C_3H_8) would lead to changes in the absorption feature depth equivalent to the single-spectrum noise level, placing a limit on the system sensitivity with no spectral averaging.

Using the same dataset, a multi-parameter spectral fit was performed independently on each spectrum, and concentration values for carbon dioxide and water (both present in ambient air) obtained, resulting in values of 401 ± 11 ppm (CO_2) and 1.47 ± 0.12 % (H_2O). The higher standard deviation for water is a result of the spectrometer being unable to fully resolve its complex line structure, resulting in spectrum-to-spectrum fitting differences, which are not as severe when fitting carbon dioxide's simpler absorption spectrum.

4. Gas localisation and mapping

4.1 Simultaneous propane and carbon dioxide point-source localisation

The ability of the system to localize a point-source gas emission was investigated for two gases: carbon dioxide, which is naturally present at high levels (400 ppm) in the atmosphere and propane, which has no natural background level. Carbon dioxide and propane are denser than air and have nearly identical molecular masses (propane, 44.1 g mol^{-1}; carbon dioxide 44.01 g mol^{-1}). Both gases were released through collocated hoses which were elevated 2 m above the ground. The UAV was flown at a height of 4 m, allowing a safety margin to avoid collisions with the gas apparatus. Figure 2 presents gas concentration maps prepared by Bayesian interpolation of concentration data obtained during an autonomous flight in which the drone surveyed the release of propane and carbon dioxide in a rectangular 720-m^2 area in the form of five 32-m-long parallel paths, each separated by 5.6 m, as illustrated in Figs. 2(a) and 2(d). Infrared spectra were recorded continuously at intervals of 0.7 seconds, corresponding to a spatial sampling resolution of 0.7 m when the drone ground speed was 1 m s^{-1}. The peak concentrations recorded were 362 ppm for propane and 677 ppm for carbon dioxide. The Bayesian interpolation of the data using a Gaussian process and accompanying uncertainty quantification is shown for propane in Figs. 2(b) and 2(e) and for carbon dioxide

in Figs. 2(c) and 2(f). The locations of the peak concentrations inferred from the interpolation are consistent to within 1.5 m.
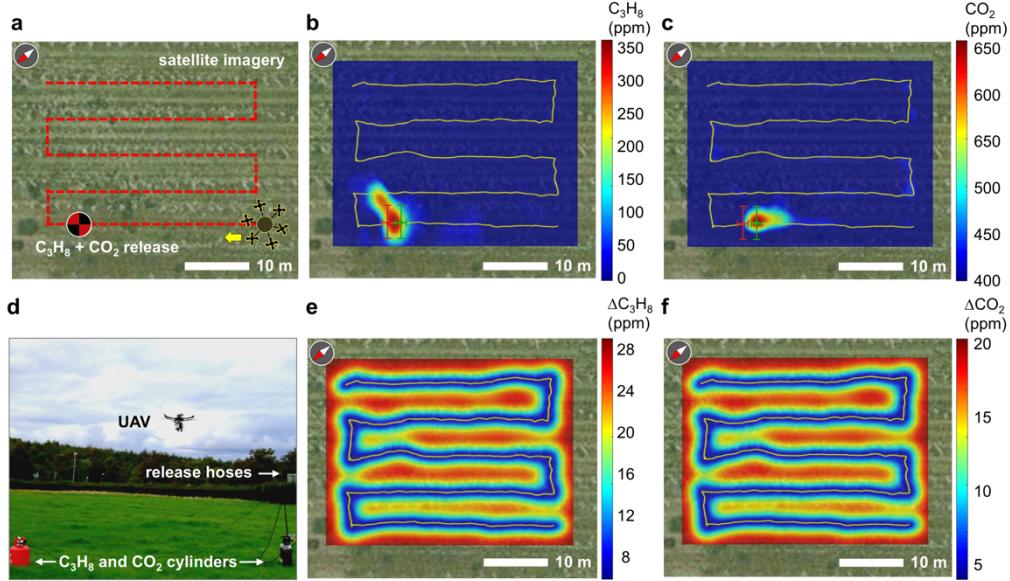

Fig. 2. Localisation of point sources of gas emissions. (a) Flight plan and (d) site image, showing the location of the propane and carbon dioxide gas sources. (b, c) Gas concentration and (e, f) accompanying uncertainty maps prepared by Bayesian interpolation of the recorded concentration data for propane and for carbon dioxide. The maximum likelihood locations of the carbon dioxide and propane sources are denoted, respectively, by the green and red crosses, with the error bars being the spatial sampling resolution. Satellite imagery ©2018 Google, used with permission under Google Terms of Service.

4.2 Mapping carbon-dioxide and humidity distribution from combustion

Under manual flight conditions we surveyed the carbon dioxide and water vapor distribution of a large-scale emission from two dung fires which had been burning for several hours, depicted in Fig. 3(a). This scenario is distinct from that of point-source localization because the gas is mixed throughout a greater volume of air, making it more likely to interact with the UAV's onboard sensor, but accompanied by the likelihood that the peak concentration levels may be considerably lower. During the flight time of four minutes we recorded 330 infrared spectra, concentrating on locations closer to the fires and observing changes in the concentrations of ambient carbon dioxide and water vapor, both of which are expected as combustion products. Bayesian interpolation was used to reconstruct estimates of the gas distribution from the irregularly sampled concentration measurements available from manual flight and the resulting concentration maps for carbon dioxide and water vapor are shown in Figs. 3(b) and 3(c). The water vapor and carbon dioxide maps show some correlation, with the increase above ambient levels being smaller for water vapor than carbon dioxide because of its larger natural background level. Uncertainty quantification maps obtained from the Gaussian process (Figs. 3(d) and 3(e)) showed typical uncertainties of 10 ppm for carbon dioxide and 5 ppm for water vapor in locations close to the sampling points.
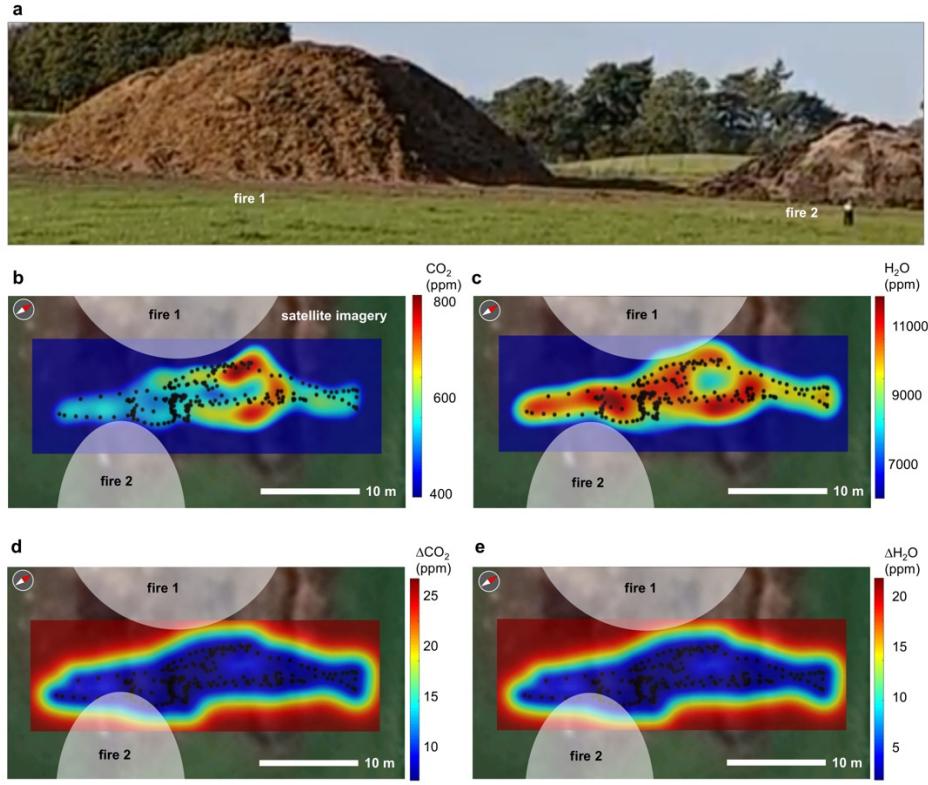
Fig. 3. Mapping atmospheric carbon dioxide and water-vapor distributions. (a) Site image illustrating the two dung-heap fires, between which the UAV was flown. No flames were visible from the fires. (b, c) Concentration maps produced from data recorded for (b) carbon dioxide and (c) water vapor during manual flight between two dung fires. Sampling points are shown in black. (d, e) Corresponding gas concentration uncertainty maps for (d) carbon dioxide and (e) water vapor, obtained from the Gaussian-process fitting. Satellite imagery ©2018 Google, used with permission under Google Terms of Service.

4.3 Multi-species spectral fitting

High resolution experimental data from the Pacific Northwest National Laboratory (PNNL) database [17] provided the basis for the spectral absorption fitting. PNNL absorbance spectra for propane, carbon dioxide and water, measured at a 0.1-cm^{-1} resolution for a 1-m path at 1 ppm, were corrected for path length and instrument resolution and combined with an envelope function $I_o(\tilde{v})$ to model the measured transmission spectrum as the following function:

$$I(\tilde{v}) = I_o(\tilde{v}) \cdot 10^{A(\tilde{v})} \tag{1}$$

where the total absorbance is defined as,

$$A(\tilde{v}) = A_{CO_2}(\tilde{v}) + A_{C_3H_8}(\tilde{v}) + A_{H_2O}(\tilde{v}) \tag{2}$$

and for each species,

$$A_X(\tilde{v}) = A_{PNNL}(\tilde{v}) \otimes \sigma(\tilde{v}) L_m C_{PPM} \tag{3}$$

where A_{PNNL} is the original PNNL absorbance data, σ is the spectrometer instrument line function, L_m is the spectrometer path length in metres, and C_{PPM} is the fitted concentration in parts per million. The concentrations of propane, carbon dioxide and water were free parameters in the fit, and the modelled spectrum was iterated using Matlab's Nelder-Mead algorithm to minimise the root mean square difference with the measured spectrum from the drone, $I_{UAV}(\tilde{v})$. The envelope function was simultaneously fitted for each spectrum as a multi-point spline curve and the instrument line function was fitted as a $sinc^2(v)$ function corresponding to the apodization window used.

Figure 1 shows an example of applying the fitting procedure to a spectrum recorded during a point-source localization flight and simultaneously exhibiting absorption features for carbon dioxide, propane and water. The fitted and measured spectra are shown together in Fig. 1(e), followed in Figs. 1(f)–1(i) by the separate components (envelope and transmittance spectra) used to construct the fit. The fitting residuals are shown in Fig. 1(j) and provide an estimate of the signal:noise performance of the system (see Section 3).

4.4 Source localization using Bayesian interpolation

To address the problem of interpolating over the area of interest from a set of sparse measurements, we used a Gaussian process (GP) [18]. A GP is defined as a distribution of functions, realized by drawing samples from a high (infinite) dimensional normal distribution. As such, a GP is defined by a mean and covariance function, which can in turn produce an arbitrarily high-dimensional mean kernel and covariance matrix for the normal distribution. By using an appropriate kernel, a useful prior over the functions can be defined, e.g. describing a gas distribution which is a smooth function of time and space. This is one of the reasons that GPs have widely been used by the sensing community [19,20], in addition to their probabilistic output allowing for performing active sensing and quantifying the certainty of the predictions.

Specifically, we implemented a GP with a zero mean function and a radial basis function kernel, horizontal length scale of $l = 0.0001$, noise $\sigma_f = 1$ and vertical length scale $\sigma_v = 1$. First, we normalized the data: for CO_2 sensing we subtracted 400 ppm (the typical background level) and divided by 1000 to give a range between zero and one. For propane no background level exists and we simply divided the acquired ppm concentrations by 2000. We fitted a GP with the above mentioned mean and kernel functions, results of which can be seen in Fig. 2. The interpolation closely matched the ground truth location of the source and the GP fit accounts for consecutive high readings where the peak source is at an unvisited location.

5. Discussion

The correlation between the carbon dioxide and propane maps in Fig. 2 clearly indicates the benefits of this measurement approach. Broadband infrared spectroscopy infers gas concentrations from a single universal measurement based on the abundance of gas molecules in a common sensing path, eliminating systematic errors resulting from inconsistencies in sampling multiple gas species using discrete sensors, as well as issues associated with cross-calibrating sensitivities and response times of different sensor types. The slight differences between the maps in Fig. 2 are attributable to the fact that the propane and carbon dioxide plumes were released in opposite directions, leading to differences in their initial dispersal conditions. Nonetheless, in both cases the maximum-likelihood location of the point source was consistent to within 1.5 m. The differences between point-source localization and gas distribution mapping are evident when Figures 2 and 3 are compared. When surveying the point-source emissions, gas was detected only within a 5-m range of the sources, however the survey of the emissions from the dung fires (Fig. 3) indicates, as expected, a much more widespread distribution of the combustion products.

The ability to record multi-species gas data rapidly and during normal flight sets our results apart from previous approaches. The benefit of using a fast optical sensor which can

acquire data as the drone is moving can be understood by comparison with earlier work in which a UAV instrumented with an electrochemical CO_2 sensor was used to survey a 5 m $\times$ 20 m area [21]. Here, the slow response time of the sensor made it necessary to hover the drone for 20 seconds at every sampling point, making the data acquisition time consuming, delivering sparse spatial sampling, and perturbing the gas distribution under investigation, leading to inconsistent results.

The signal:noise performance of the system is limited by a number of factors but is predominantly due to intensity fluctuations of the thermal light source and the noise floor of the mercury cadmium telluride detector. The values for propane and carbon dioxide can be used to estimate the sensitivity of the system to gases not evaluated in this study but of interest in pollution monitoring or environmental sensing. For example, UAV measurements of CO_2:SO_2 ratios in volcanic gas emissions have been shown to be correlated with volcanic activity. The infrared absorption cross-section of SO_2 is slightly higher than propane, and modelling using PNNL data [17] implies a sensitivity of <17 ppm would be expected. Similarly, NO_2 exhaust emission from cars and ships should be detectable with a sensitivity of < 11 ppm.

The length and position of the sensing path of the infrared spectrometer impose a fundamental limit on the measurement sensitivity. Computational fluid dynamics models of quadcopter UAVs [22], confirmed experimentally [16], imply only two viable mounting locations for gas sensors, namely at the centre of the UAV or several tens of cm away from it. The natural payload site on many drones – including the DJI M600 used in our experiments – is underneath the main body, but hexacopter simulations reveal a conical volume underneath the drone where the static pressure is close to zero, leading to poor air circulation into this region and effectively screening it from nearby gas [23]. As described in Section 2, we addressed this by using a C-shaped sensing path, however optimal gas sensing would only be expected if the entire path were situated on top of the central body of the drone. Advances in compact, lightweight multi-pass cells [24] make it feasible to achieve a 10-m laser path in a cell with a mass of 200 g and a diameter of 150 mm [25], and may eventually be extendable to broadband thermal sources which lack the spatial coherence of a laser. Using lightweight construction materials such as carbon-fiber rods, a mast design may also be feasible, in which the sensing path projects upwards from the drone body and terminates either at a retroreflector or a detector.

Current regulations in many countries require the UAV to be under the control of a pilot at all times and in visual line of sight, limiting the degree of autonomy which can be conferred to the drone. The experiments we performed used pre-programmed paths, allowing the drone behavior to be known in advance, even when the flight itself was autonomous. An active sensing approach, where the drone utilizes in-flight gas concentration information to adapt its flight plan in real time, could allow the UAV to climb a concentration gradient to quickly locate a gas source without a wide-area survey [26]. Alternatively, a UAV could be programmed to track a concentration iso-contour in order to demarcate a safe standoff distance from a source of gas. Future UAVs equipped with advanced collision avoidance systems may be permitted to operate beyond visual line of sight, where the advantages of full autonomy can be exploited.

6. Summary

The results presented here are, to our knowledge, the first demonstration of drone-based broadband infrared atmospheric spectroscopy. The long-wave infrared coverage accesses far higher molecular absorption cross-sections than are available at shorter wavelengths, achieving sub-40-ppm sensitivity for in-flight gas sensing using only a short sensing path. The sensing capabilities are enhanced by an innovative gas concentration mapping approach, which leverages machine learning techniques to obtain concentration maps from spatially sparse datasets and accompanying uncertainty quantification.

References

1. M. V. Ramana, V. Ramanathan, D. Kim, G. C. Roberts, and C. E. Corrigan, "Albedo, atmospheric solar absorption and heating rate measurements with stacked UAVs," Quarterly Journal of the Royal Meteorological Society **133**(629), 1913–1931 (2007).
2. O. Evangelatos and J. Rolim, "An airborne wireless sensor system for near-real time air pollution monitoring," Sensors and Transducers **189**, 12–21 (2015).
3. A. J. S. McGonigle, A. Aiuppa, G. Giudice, G. Tamburello, A. J. Hodson, and S. Gurrieri, "Unmanned aerial vehicle measurements of volcanic carbon dioxide fluxes," Geophysical Research Letters **35**(6), (2008).
4. M. Alvarado, F. Gonzalez, A. Fletcher, and A. Doshi, "Towards the Development of a Low Cost Airborne Sensing System to Monitor Dust Particles after Blasting at Open-Pit Mine Sites," Sensors **15**(8), 19667–19687 (2015).
5. N. Mölders, M. K. Butwin, J. M. Madden, H. N. Q. Tran, K. Sassen, and G. Kramm, "Theoretical Investigations on Mapping Mean Distributions of Particulate Matter, Inert, Reactive, and Secondary Pollutants from Wildfires by Unmanned Air Vehicles (UAVs)," Open Journal of Air Pollution **4**(3), 149–174 (2015).
6. W. A. Harrison, D. J. Lary, B. J. Nathan, and A. G. Moore, "Using Remote Control Aerial Vehicles to Study Variability of Airborne Particulates," Air, Soil and Water Research **8**, ASWR.S30774 (2015).
7. S. Martin, J. Bange, and F. Beyrich, "Meteorological profiling of the lower troposphere using the research UAV "M2AV Carolo,"" Atmospheric Measurement Techniques **4**(4), 705–716 (2011).
8. T. S. Bates, P. K. Quinn, J. E. Johnson, A. Corless, F. J. Brechtel, S. E. Stalin, C. Meinig, and J. F. Burkhart, "Measurements of atmospheric aerosol vertical distributions above Svalbard, Norway, using unmanned aerial systems (UAS)," Atmospheric Measurement Techniques **6**(8), 2115–2120 (2013).
9. B. Altstädter, A. Platis, B. Wehner, A. Scholtz, A. Lampert, N. Wildmann, M. Hermann, R. Käthner, J. Bange, and H. Baars, "ALADINA – an unmanned research aircraft for observing vertical and horizontal distributions of ultrafine particles within the atmospheric boundary layer," Atmospheric Measurement Techniques Discussions **7**(12), 12283–12322 (2014).
10. T. Villa, F. Gonzalez, B. Miljievic, Z. Ristovski, and L. Morawska, "An Overview of Small Unmanned Aerial Vehicles for Air Quality Measurements: Present Applications and Future Prospectives," Sensors **16**(7), 1072 (2016).
11. M. Rossi and D. Brunelli, "Autonomous Gas Detection and Mapping With Unmanned Aerial Vehicles," IEEE Transactions on Instrumentation and Measurement **65**(4), 765–775 (2016).
12. B. J. Nathan, L. M. Golston, A. S. O'Brien, K. Ross, W. A. Harrison, L. Tao, D. J. Lary, D. R. Johnson, A. N. Covington, N. N. Clark, and M. A. Zondlo, "Near-Field Characterization of Methane Emission Variability from a Compressor Station Using a Model Aircraft," Environmental Science & Technology **49**(13), 7896–7903 (2015).
13. R. Knake and P. C. Hauser, "Sensitive electrochemical detection of ozone," Analytica Chimica Acta **459**(2), 199–207 (2002).
14. C. Wang, L. Yin, L. Zhang, D. Xiang, and R. Gao, "Metal Oxide Gas Sensors: Sensitivity and Influencing Factors," Sensors **10**(3), 2088–2106 (2010).
15. G. Saggiani, F. Persiani, A. Ceruti, P. Tortora, E. Troiani, F. Giuletti, S. Amici, M. Buongiorno, G. Distefano, G. Bentini, M. Bianconi, A. Cerutti, A. Nubile, S. Sugliani, M. Chiarini, G. Pennestri, S. Petrini and D. Pieri, "A UAV system for observing volcanoes and natural hazards. American Geophysical Union, Fall Meeting 2007, Washington, DC, USA. Abstract GC11B-05 (2007).
16. J. Roldán, G. Joossen, D. Sanz, J. del Cerro, and A. Barrientos, "Mini-UAV Based Sensory System for Measuring Environmental Variables in Greenhouses," Sensors **15**(2), 3334–3350 (2015).
17. S. W. Sharpe, T. J. Johnson, R. L. Sams, P. M. Chu, G. C. Rhoderick, and P. A. Johnson, "Gas-Phase Databases for Quantitative Infrared Spectroscopy," Applied Spectroscopy **58**(12), 1452–1461 (2004).
18. C. E. Rasmussen, "Gaussian Processes in Machine Learning," in Advanced Lectures on Machine Learning (Springer Berlin Heidelberg, 2004), pp. 63–71.
19. A. Krause, A. Singh, and C. Guestrin, "Near-optimal sensor placements in Gaussian processes: Theory, efficient algorithms and empirical studies," J. Machine Learning Research **9**, 235–284 (2008).
20. J. Le Ny and G. J. Pappas, "On trajectory optimization for active sensing in Gaussian process models," in Proceedings of the 48h IEEE Conference on Decision and Control (CDC) Held Jointly with 2009 28th Chinese Control Conference (IEEE, 2009).
21. P. Neumann, S. Asadi, A. Lilienthal, M. Bartholmai, and J. Schiller, "Autonomous Gas-Sensitive Microdrone: Wind Vector Estimation and Gas Distribution Mapping," IEEE Robotics & Automation Magazine **19**(1), 50–61 (2012).

22. G. T. Poyi, B. Wiggins, M. H. Wu, and A. Bousbaine, "Validation of a quad-rotor helicopter Matlab/Simulink and Solidworks models," in IET Conference on Control and Automation 2013: Uniting Problems and Solutions (Institution of Engineering and Technology, 2013).

23. P. Y. Haas, C. Balistreri, P. Pontelandolfo, G. Triscone, H. Pekoz, and A. Pignatiello, "Development of an unmanned aerial vehicle UAV for air quality measurement in urban areas," in 32nd AIAA Applied Aerodynamics Conference (American Institute of Aeronautics and Astronautics, 2014).

24. B. Tuzson, M. Mangold, H. Looser, A. Manninen, and L. Emmenegger, "Compact multipass optical cell for laser spectroscopy," Optics Letters **38**(3), 257 (2013).

25. M. Graf, L. Emmenegger, and B. Tuzson, "Compact, circular, and optically stable multipass cell for mobile laser absorption spectroscopy," Optics Letters **43**(11), 2434 (2018).

26. M. Asenov, M. Rutkauskas, D. Reid, K. Subr, and S. Ramamoorthy, "Active Localization of Gas Leaks using Fluid Simulation," IEEE Robotics and Automation Letters 1–1 (2019).